Theory of the coalescence of two spherical liquid drops at early times

R. Brandão[1]†, J. Eggers[1]‡, M.A. Fontelos[2], J.E. Sprittles[3]

[1]School of Mathematics, University of Bristol, Fry Building, Woodland Road, Bristol BS8 1UG, United Kingdom

[2] Instituto de Ciencias Matemáticas, (ICMAT, CSIC-UAM-UCM-UC3M), C/ Serrano 123, 28006 Madrid, Spain

[3] Mathematics Institute, University of Warwick, Coventry, CV4 7AL, United Kingdom

(Received xx; revised xx; accepted xx)

We consider the dynamics of two equal, spherical liquid drops of Newtonian fluid, brought into contact at a negligible speed, and merging driven by surface tension. The effects of an outer fluid or that of gravity are disregarded, so that the entire motion is determined uniquely by the Ohnesorge number $\mathrm{Oh} = \eta/\sqrt{\rho\gamma R}$, where η is the viscosity, ρ the density, γ the surface tension, and R the drop radius. Using methods of matched asymptotics, in the limit that the minimum radius r_0 of the bridge connecting the drops is much smaller than the initial drop radius, we compute the dynamics for $r_0(t)$, as well as the shape of the gap between the drops. For very early times, the translational motion of the drops along the axis of symmetry is arrested by inertia, which affects the shape of the scaling function describing the gap on the scale of r_0. For $r_0 \approx \sqrt{\ln \mathrm{Oh}}/\mathrm{Oh}$, the motion crosses over to an entirely viscous similarity solution, passing through a sequence of time-dependent scaling functions, which we compute. Our results agree well with full numerical simulations of the Navier-Stokes equation, as well as experiment.

1. Introduction

Coalescence is one of the fundamental processes that change the topology of a free surface flow, and as a result has generated long-standing interest (Eggers *et al.* 2025). Throughout this paper we will focus on the idealized problem of two drops of Newtonian fluid in a state of equilibrium, being brought into contact at vanishing relative speed. Any effect of an outer fluid (or gas) is neglected, as well as any detail of the reconnection process (both of which may influence the early stages of coalescence (Eggers *et al.* 1999; Deblais *et al.* 2025). We assume the remainder of the evolution to be described by the Navier-Stokes equation with surface tension.

A significant step forward in the understanding of this problem was made by Hopper (1993*b*, 1991, 1993*c*), who solved the two-dimensional Stokes flow problem, in which two "drops" (cylinders) of radius R merge under the action of surface tension. This was achieved by recognizing that the coalescence dynamics is described by a sequence of simple rational functions, which map the flow domain, represented in the complex plane, onto the unit circle. In the limit of long times, the two drops merge into a single drop of radius $\sqrt{2}R$. We however focus on the limit of early times, for which the bridge radius $r_0 \ll R$. In contrast to an earlier proposal by Frenkel (1945), Hopper's results show that r_0 grows almost linearly in time, with the slope behaving logarithmically: $\dot{r}_0 \propto t \ln t$.

† present address: Department of Mathematics, University of British Columbia, Vancouver, BC V6T 1Z2, Canada

‡ Email address for correspondence: jens.eggers@bristol.ac.uk

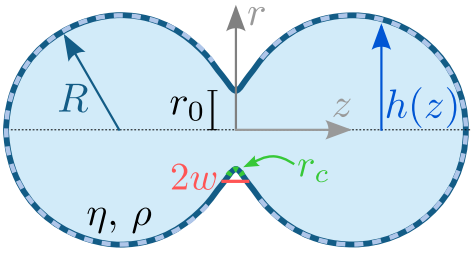

FIGURE 1. A sketch of the early stages of coalescence, showing two spherical drops of radius R, viscosity η, and density ρ, shortly after they have been brought into contact; the shape is described by $h(z)$, where z is the coordinate along the axis of symmetry. The minimum radius of the bridge connecting the drops is r_0 and its typical half-width is $w = r_0^2$, while the radius of curvature at the tip is $r_c \propto r_0^3$.

In Eggers *et al.* (1999) it was shown that the dynamics of the liquid bridge joining two spherical viscous drops is in fact the same as in the two-dimensional case to leading order. The reason is that the motion is driven by the highly localized curvature at the tip of the bridge. Since the size of the tip is small compared to the bridge radius itself, the curvature at which the tip wraps around the bridge is small compared to the driving curvature, making the local problem effectively two-dimensional. For small Oh (small viscosity), the motion is initially viscous, and crosses over to inviscid motion at $r_0 \approx \mathrm{Oh}R$ (Paulsen *et al.* 2011), after which $r_0 \propto t^{1/2}$. These trends have been well verified experimentally (Menchaca-Rocha *et al.* 2001; Paulsen *et al.* 2011; Paulsen 2013; Xia *et al.* 2019; Thoroddsen *et al.* 2005; Aarts *et al.* 2005), but experiments are not sufficiently resolved to identify the expected logarithmic corrections in the viscous regime (Eggers *et al.* 2025). In the present paper, we will be concerned exclusively with a regime in which the motion on the scale of r_0 is viscously dominated.

But regardless of how small r_0, Paulsen *et al.* (2012) proposed that inertia always changes the early-time dynamics of r_0, turning a logarithmically varying slope into a purely linear behavior. This claim was based on the idea that viscous coalescence is associated with a small translational acceleration of the drops in the axial direction, which is suppressed by the presence of inertia. However, subsequent numerical simulations (Sprittles & Shikhmurzaev 2012*a*, 2014) showed no evidence of a linear regime, and it was confirmed later (Anthony *et al.* 2020) that the appearance of a linear regime in the earlier numerical simulations was due to a non-vanishing shift in the drops' initial conditions.

Here, we begin with a more detailed analysis of the early stages of viscous drop coalescence in three dimensions, on the basis of the Stokes equation. We show that the gap between the two drops is described by a similarity solution, which we calculate. As a result, we obtain a more accurate description of the tip velocity $\dot{r}_0$, beyond the leading order calculated in Eggers *et al.* (1999). In doing so, we exploit the slenderness of the gap between the two drops, as proposed in Howison *et al.* (1997), and building on unpublished earlier work (Munro 2018; Gillow 1998; Morgan 1994) as well as work on *stationary* cusps (Jeong & Moffatt 1992; Eggers 2023; Brandão *et al.* 2026).

Next, we include the effects of inertia in the regime of large but finite Oh. As suggested by Paulsen *et al.* (2012), the dominant inertial effects are contained in the accelerated translational motion of the drops along the axis of symmetry, without other deformation. By taking into account the relevant forces quantitatively, we calculate the temporal evolution of the similarity profile for any value of Oh. We also compute the crossover in the dynamics of r_0, which occurs at $r_0 \approx \sqrt{\ln \mathrm{Oh}}/\mathrm{Oh}$.

The geometry of the problem is shown in Fig. 1. From now on, we will take the initial radius R of the drops as unit of length, and $R\eta/\gamma$ as unit of time. As shown in Fig. 1, $h(z)$ denotes the radial position of the free surface in cylindrical coordinates. Then the Navier-Stokes equation for the axisymmetric, uncompressible velocity field $\mathbf{v}(z,r) = v_r\mathbf{e}_r + v_z\mathbf{e}_z$ with pressure $p(z,r)$ becomes

$$\frac{1}{\mathrm{Oh}^2}\left(\frac{\partial \mathbf{v}}{\partial t} + (\mathbf{v}\cdot\boldsymbol{\nabla})\mathbf{v}\right) = \boldsymbol{\nabla}\cdot\boldsymbol{\sigma} = -\boldsymbol{\nabla}p + \triangle\mathbf{v}, \quad \boldsymbol{\nabla}\cdot\mathbf{v} = 0, \tag{1.1}$$

to be satisfied in the interior of the drops, and where $\boldsymbol{\sigma}$ is the stress tensor. With $\mathbf{n}$ being the outward normal and κ twice the mean curvature, the stress boundary condition expressing the balance with surface tension becomes

$$\mathbf{n}\cdot\boldsymbol{\sigma} = -\kappa\mathbf{n} \equiv -\left(\frac{1}{(1+h'^2)^{1/2}} - \frac{h''}{(1+h'^2)^{3/2}}\right)\mathbf{n}, \tag{1.2}$$

where a prime denotes the derivative with respect to the argument. Finally, the kinematic boundary condition for the motion of the free surface can be written as

$$\frac{\partial h}{\partial t} + v_z h' = v_r|_{r=h}. \tag{1.3}$$

In the limit in which viscous forces become dominant, (1.1) can be replaced by the Stokes equation

$$\boldsymbol{\nabla}p = \triangle\mathbf{v}, \quad \boldsymbol{\nabla}\cdot\mathbf{v} = 0. \tag{1.4}$$

1.1. *Computational Approach*

We consider the full problem, consisting of the Navier-Stokes equations (1.1) subject to conventional boundary conditions (1.2)–(1.3) for the geometry shown in Fig. 1 (i.e. an axisymmetric coalescence with a symmetry plane at $z = 0$). In general, capturing this high-deformation free-boundary problem with the effects of viscosity, inertia and capillarity requires a computational approach. The main challenge then is to simultaneously and accurately describe both the very small spatio-temporal scales associated with the early stages of coalescence alongside the global motion of the droplets, see the *Numerical Methods* section in Eggers *et al.* (2025). To do so, we use the arbitrary Lagrangian-Eulerian finite element method, which has been the most successful tool used for resolving capillary flows exhibiting singularities, as reviewed in Anthony *et al.* (2023). This permits a multiscale mesh to be designed that allows resolution of the bridge front's dynamics with very small elements, whilst retaining computational tractability by allowing for larger elements throughout the bulk of the droplet. The particular code used in this article was originally developed for dynamic wetting flows, with the implementation described in great detail in Sprittles & Shikhmurzaev (2012*b*), and then adapted to capture the coalescence of liquid drops in Sprittles & Shikhmurzaev (2012*a*, 2014) where it has been thoroughly tested. Notably, in Fig.2 of Eggers *et al.* (2025) the code has been shown to describe experimental data for the coalescence process across many decades of Oh and r_0.

Of particular relevance here is the initiation of the simulation from a bridge of small but finite width, which is discussed in *Numerical Methods* of Eggers *et al.* (2025). Here, simulations are initiated with a bridge of size $r_0 = 10^{-4}$ and results in Sprittles & Shikhmurzaev (2012*a*) have shown that any contamination from the initial conditions can be neglected from $r_0 = 10^{-3}$ onwards.

1.2. *Overview*

In the next section, we discuss the three asymptotic regions needed to describe the asymptotics of viscous coalescence, shown in Fig. 2: the tip region of highest curvature, the scale of the liquid bridge between the two drops, and finally the scale of the drops themselves. Matching the regions together, we are able to treat the case of infinite Oh (no inertia). In Section 3, we formulate the force balance between the liquid bridge and the translational drop motion, and integrate the resulting equations of motion in terms of the parameters of the liquid bridge. Finally, we discuss our results.

2. Structure of the solution

The asymptotic solution can be broken up into three different regions, which are treated separately in the subsections below. We will then show how they can be matched together, to obtain a complete solution. To understand the origin of the length scales involved in the different regions, we note that the initial condition for the drop shape is

$$h_{in}(z) = \sqrt{1-(1-z)^2}, \tag{2.1}$$

for the right-hand drop, see Fig. 1. The other side follows from symmetry. Near the point of contact, this corresponds to $h \approx \sqrt{2z}$, or $w = r^2/2$, for the half-width of the gap between the two drops.

Now imagine coalescence has progressed to produce a bridge of radius r_0 between the two drops. Then at this scale the typical width between the two drops will be r_0^2. This suggests the existence of a similarity solution describing the shape of the gap in the form

$$w(r) = r_0^2 W(\xi), \quad \xi \equiv \frac{r}{r_0}. \tag{2.2}$$

For this solution to be regular at the tip, where the shape is parabolic, we must have $W \approx a\xi^{1/2}$, where a is a constant, so that the radius of curvature r_c at the minimum becomes

$$r_c^{-1} = \frac{d^2 r}{dz^2} = \frac{1}{r_0^3}\left(W^{-1}\right)'' = \frac{2}{a^2 r_0^3}.$$

In other words, the typical size of the tip becomes $r_c \approx r_0^3 \ll r_0^2$, as pointed out in Eggers *et al.* (1999).

To summarize, four different length scales come into play. The tip of the bridge connecting the two drops has a typical size r_0^3; the bridge has a radial extension of $r_0 \ll 1$ and a typical width r_0^2; finally, the drops themselves are of size unity. Throughout the construction of our solution, we argue that for early times, inertia is negligible and we can use Stokes' equation (1.4). The only inertial effects come into play through a translational motion of the drops, as discussed in Sec. 3.

2.1. *Tip scale*

On the scale of the tip size $r_c \propto r_0^3$, the interface has the form of a parabola, as shown in Fig. 2. Since the tip of the bridge traces out a ring of size r_0, much larger than the tip size r_0^3, the local solution is effectively two-dimensional. Thus for the inner region, one can use an exact solution of the two-dimensional Stokes equation, which corresponds to a uniformally translating parabolic interface. To recover the far field of the velocity, one can integrate the two-dimensional solutions over a ring of radius r_0.

As indicated in Fig. 2, in units of r_c the interface has the form

$$Y = \sqrt{2X}, \text{with } X = \frac{x-r_0}{r_c}, \quad Y = \frac{y}{r_c}, \tag{2.3}$$

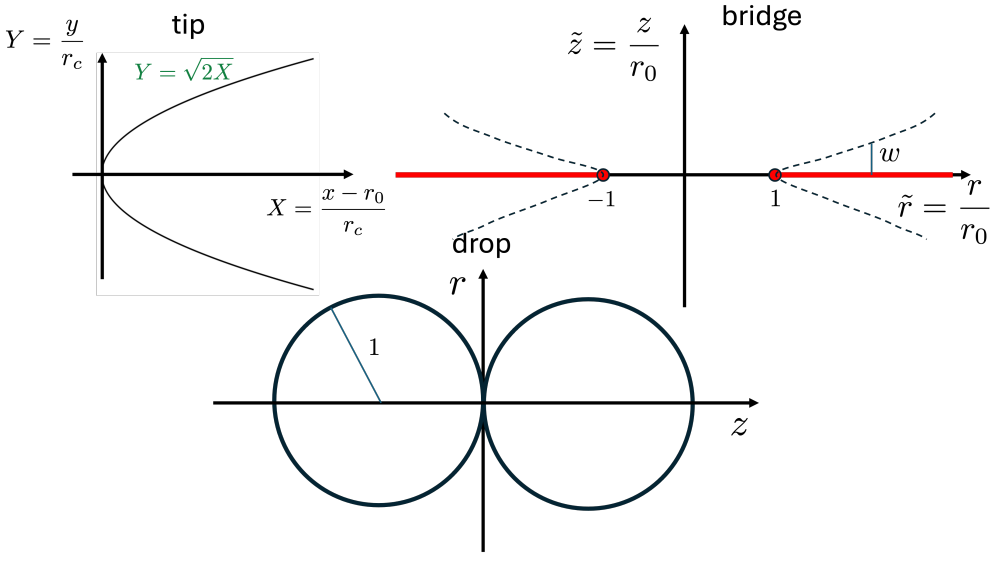

FIGURE 2. The three different asymptotic regions. On the scale of the tip curvature $r_c^{-1} \sim r_0^{-3}$, the interface is a (locally two-dimensional) parabola. On the scale of the bridge radius r_0, the gap between the two drops, which is of size $w \sim r_0^2$, collapses to two lines. On the scale of the drop size itself, two spheres of unit radius touch.

where the tip has been placed at the origin of the coordinate system. The corresponding Stokes flow, driven by the surface tension of the interface, has been calculated by Hopper (1993*a*), mapping the exterior of the parabola (the flow domain) onto the upper half plane:

$$X + iY = 2v(\zeta) \equiv 2\left(\zeta^2 + i\zeta\right), \tag{2.4}$$

where ζ real corresponds to the free surface (2.3). An explicit solution can be found in the Goursat representation (Jeong & Moffatt 1992), in which the stream function of the flow is written in terms of two holomorphic functions f and g:

$$\psi = \Im\left\{f(z) + \bar{z}g(z)\right\}. \tag{2.5}$$

As shown by Hopper (1993*a*), the steady flow around the parabola (2.4) is given by

$$f = \frac{i}{2}v'(\zeta)\bar{v}(\zeta)G(\zeta), \quad g = -\frac{i}{2}v'(\zeta)G(\zeta), \tag{2.6}$$

where

$$G = \frac{1}{2\pi i\sqrt{1+4\zeta^2}}\ln\left(\frac{2\zeta - \sqrt{1+4\zeta^2}}{2\zeta + \sqrt{1+4\zeta^2}}\right),$$

and $\bar{v}(\zeta) = \overline{v(\bar{\zeta})}$ is the conjugate function. Brandão *et al.* (2026) show that this results in a tangential velocity along the interface already given by Eggers (2023):

$$u_0(\phi) = -\frac{1}{\pi}\ln\left(\sqrt{1+\phi^2} + \phi\right), \quad \phi = \sqrt{2X}. \tag{2.7}$$

In the far field, using the slenderness of the parabola, the x-velocity becomes (Brandão *et al.* 2026):

$$u = -\frac{\ln(8X)}{2\pi}. \tag{2.8}$$

This result is valid for $r_0^3 \ll r - r_0 \ll r_0$, on a scale much larger than the size of the tip on one hand, and on a scale where the curvature of the tip of the bridge, as it curves around the z-axis, is not yet felt on the other. The velocity (2.8) is also the far field velocity of a stokeslet (the solution to the Stokes equation in response to a point force, (Pozrikidis 1992)) of strength 2 in two dimensions, pulling in the x-direction. The force comes from the pull of the two sides of the interface, generated by surface tension.

However, in order to find how the tip of the bridge moves in the radial direction, we have to include all contributions coming from the scale of r_0, i.e. coming from the ring of forces traced out by the meniscus. To this end we compare (2.8) to the velocity generated by the forcing $2\delta(r-r_0)\delta(z)\mathbf{e}_r$ coming from the tip. The result, using Hankel transforms, is (Eggers *et al.* 1999):

$$v_r(r,z) = \frac{r_0}{2}\int_0^\infty J_1(kr)J_1(kr_0)(1-kz)e^{-kz}\mathrm{d}k \tag{2.9}$$

$$v_z(r,z) = -\frac{r_0}{2}\int_0^\infty J_0(kr)J_1(kr_0)kze^{-kz}\mathrm{d}k, \tag{2.10}$$

where the J_n are Bessel functions. Here we only need the radial velocity in the $z = 0$ plane, which for $r > r_0$ becomes (Gradshteyn & Ryzhik 1980)

$$v_r(r) = \frac{r_0}{2}\int_0^\infty J_1(kr)J_1(kr_0)\mathrm{d}k = \frac{1}{\pi}\left[K\left(\frac{r_0}{r}\right) - E\left(\frac{r_0}{r}\right)\right], \tag{2.11}$$

where $K(m)$ and $E(m)$ are elliptic integrals of the first and second kinds, respectively, as defined in Gradshteyn & Ryzhik (1980).

In order to compare to the locally two-dimensional result (2.8), we expand (2.11) near $r \approx r_0$:

$$v_r(r) \approx \frac{1}{2\pi}\left[-\ln\frac{r-r_0}{r_0} + 3\ln 2 - 2\right]. \tag{2.12}$$

Since (2.8) is valid in a frame of reference in which the tip of the cusp is stationary, while in a laboratory frame the tip moves at a speed $\dot{r}_0$ outwards, in the range $r_0^3 \ll r - r_0 \ll r_0$ (2.12) must equal (2.8), with $X = (r - r_0)/r_0^3$, and $\dot{r}_0$ added to it. Clearly, the two expressions match if we identify

$$\dot{r}_0 = \frac{1}{2\pi}\ln\frac{64r_0}{e^2 r_c}, \tag{2.13}$$

which agrees with the leading order result of Eggers *et al.* (1999) as $r_0/r_c \to \infty$.

Indeed, the right hand side of (2.13) corresponds to the velocity field generated by a two-dimensional stokeslet at a distance r_c, the logarithm being cut off at r_0, the scale at which the stokeslets, located on a ring of radius r_0, cancel each other out. In addition to Eggers *et al.* (1999), we have now calculated the numerical factor inside the logarithm, which determines the vertical shift in a plot $\dot{r}_0(r_0/r_c)$. For comparison, the corresponding result in two dimensions, for the merging of two cylinders, is

$$\dot{r}_0 = \frac{1}{2\pi}\ln\frac{16r_0}{r_c}, \tag{2.14}$$

as can be checked comparing to Hopper (1990)'s exact solution, or repeating the above calculation for a pair of opposing stokeslets instead of a ring. As expected (cf. Eggers *et al.* (1999)), (2.13) and (2.14) agree to leading order in the limit $r_0/r_c \to \infty$, but the constants are different.

2.2. *Bridge scale*

The geometry on the scale of the bridge is shown in Fig. 2. Inside the fluid domain, we solve Stokes' equation (1.4) for an incompressible fluid, which can be written in terms of the streamfunction $\psi(r,z)$ satisfying $E^4\psi = 0$ (Happel & Brenner 1983), where in cylindrical coordinates the operator E^2 is defined by

$$E^2\psi = \left(\frac{\partial^2\psi}{\partial r^2} - \frac{1}{r}\frac{\partial}{\partial r} + \frac{\partial^2}{\partial z^2}\right)\psi. \tag{2.15}$$

The components of the velocity field are found from ψ using

$$v_r = \frac{1}{r}\frac{\partial\psi}{\partial z}, \quad v_z = -\frac{1}{r}\frac{\partial\psi}{\partial r}. \tag{2.16}$$

The free surface is defined by $w(r)$ for $r > r_0$, on which the stress boundary condition (1.2) holds; the kinematic boundary condition (1.3) takes the form

$$\frac{\partial w}{\partial t} + v_r\frac{\partial w}{\partial r} = v_z, \tag{2.17}$$

on the surface $z = w(r)$.

As will be confirmed self-consistently below, the width of the gap is of the form (2.2), and thus of the order r_0^2. This means when we introduce the rescaled coordinates $\tilde r = r/r_0$ and $\tilde z = z/r_0$, in the limit $r_0 \to 0$ the interface is located at $|\tilde r| > 1$, $\tilde z = 0$, corresponding to a domain with a double slit, as shown in Fig. 2. However, since we are on scale r_0, we still have to solve the full axisymmtric problem. Next, keeping in mind that (2.17) now has to be solved on the line $\tilde z = 0$, we estimate the size of the velocity field, by combining (2.17) with (2.2) to find

$$v_z \sim \frac{\partial w}{\partial t} \sim r_0\dot r_0(2W - \tilde r W').$$

Thus the velocity field has the structure $\mathbf{v} = \mathbf{v}_{\rm Stokes} + r_0\dot r_0\mathbf{V}$, or in terms of the stream function

$$\psi = \psi_{\rm Stokes} + r_0^2\dot r_0\Psi(\tilde r,\tilde z), \tag{2.18}$$

where $\psi_{\rm Stokes}$ is the streamfunction corresponding to (2.9),(2.10), coming from the asymptotics for $r \gg r_c$. The integral can be performed as (Gradshteyn & Ryzhik 1980):

$$\psi_{\rm Stokes}(\tilde r,\tilde z) = \frac{\tilde r\tilde z}{2}\int_0^\infty J_1(k\tilde r)J_1(k)e^{-k\tilde z}{\rm d}k = \frac{\tilde z\sqrt{\tilde r}}{2\pi}{\rm Q}_{\frac12}\left(\frac{1+\tilde r^2+\tilde z^2}{2\tilde r}\right), \tag{2.19}$$

where $Q_{\frac12}(x)$ is a Legendre function of half-integral degree, which can also be expressed through elliptic integrals (Abramowitz & Stegun 1968).

We only need this solution for $\tilde z = 0$, where using (2.12) we can write

$$v_r = \frac{\ln r_0}{2\pi} + r_0\dot r_0 V_r, \quad v_z = r_0\dot r_0 V_z, \tag{2.20}$$

to leading order as $r_0 \to 0$. Since $v_r\partial_r v_z \sim r_0$ and $v_z \sim r_0\dot r_0$, (2.17) simplifies to the linear equation $\partial_t w = v_z$, which in view of the similarity form (2.2) takes the form

$$2W - \tilde r W' = -\frac{1}{\tilde r}\Psi_{\tilde r}, \quad \text{on } \tilde z = 0. \tag{2.21}$$

2.3. *Basis functions*

The perturbation (V_r, V_z) satisfies Stokes' equation, i.e. we have to find a streamfunctions $\Psi(\tilde r,\tilde z)$ with $\triangle^2\Psi = 0$ in three-dimensional space, excepting $\tilde z = 0, |\tilde r| > 1$, and the

velocity components are

$$V_r = \frac{1}{\tilde{r}}\frac{\partial \Psi}{\partial \tilde{z}}, \quad V_z = -\frac{1}{\tilde{r}}\frac{\partial \Psi}{\partial \tilde{r}}. \tag{2.22}$$

On $\tilde{z} = 0, |\tilde{r}| > 1$, the solution has to satisfy the stress-free conditions $\mathbf{n} \cdot \boldsymbol{\sigma} \cdot \mathbf{n} = 0$ and $\mathbf{n} \cdot \boldsymbol{\sigma} \cdot \mathbf{t} = 0$, and on the disk $\tilde{z} = 0, |\tilde{r}| < 1$ it satisfies the symmetry conditions $V_z = 0$ and $\partial_{\tilde{z}} V_r = 0$; from this it also follows that the shear stress vanishes. Using the Stokes equation to eliminate the pressure, in summary we are looking for a solution of $E^4\Psi = 0$, subject to the conditions on $\tilde{z} = 0$:

$$\begin{cases} \Psi = 0,\ \Psi_{\tilde{z}\tilde{z}} = 0 & |\tilde{r}| < 1, \\ \tilde{r}(\Psi_{\tilde{r}}/\tilde{r})_{\tilde{r}} - \Psi_{\tilde{z}\tilde{z}} = 0,\ \Psi_{\tilde{z}\tilde{z}\tilde{z}} + 3\Psi_{\tilde{z}\tilde{r}\tilde{r}} - 3\Psi_{\tilde{z}\tilde{r}}/\tilde{r} = 0 & |\tilde{r}| > 1. \end{cases} \tag{2.23}$$

To describe the flow on the scale of the bridge, we represent this solution as a superposition of basis functions, which we discuss now.

The boundary conditions (2.23) are analogous to the stress-free and symmetry conditions imposed on a single slit when describing a stationary cusp in two dimensions (Eggers & Fontelos 2015; Brandão *et al.* 2026). Therefore we can order the basis functions of the full problem in terms of their (singular) behavior near the edge at $\tilde{z} = 0, \tilde{r} = 1$. To this end we put $\tilde{r} = 1 - \rho\cos\theta, \tilde{z} = -\rho\sin\theta$ and consider the local behavior as $\rho \to 0$. As shown in Eggers & Fontelos (2015), there are two types of solutions. The first has integer exponents ρ^n and has a streamfunction of the form

$$\Psi = \rho^n \left[\sin(n\theta) - \sin((n-2)\theta)\right], \quad n = 1, 2, \ldots, \tag{2.24}$$

counting only the non-singular solutions. The second type has half-integer scaling exponents $\rho^{n-1/2}$, with streamfunction

$$\Psi = \rho^{(2n-1)/2}\left[\sin\left(\frac{2n-1}{2}\theta\right) + \frac{2n-1}{5-2n}\sin\left(\frac{2n-5}{2}\theta\right)\right], \quad n = 1, 2, \ldots . \tag{2.25}$$

We note that the streamfunctions (2.24) satisfy $\Psi = \Psi_{\theta\theta} = 0$ at $\theta = \pi$ and the streamfunctions (2.25) satisfy $\Psi_\theta = \Psi_{\theta\theta\theta} = 0$ at $\theta = \pi$. Again, we only have included solutions which are not too singular at the origin. Finally, there is

$$\Psi = -\frac{\rho\sin\theta}{4\pi}\ln\left(\frac{\rho}{a}\right), \tag{2.26}$$

where a is a positive constant. The logarithmic solution (2.26) (Brandão *et al.* 2026) corresponds to the velocity field generated by a point force of unit strength, pulling in the x-direction, i.e. a stokeslet.

As shown in more detail in Appendix A, we find a solution satisfying boundary conditions (2.23) for each of the possible local behaviors of ψ near the tip $\tilde{r} = 1, \tilde{z} = 0$, as described by (2.24) or (2.25). The three-dimensional axisymmetric solution corresponding to the stokeslet (2.26) is (2.19), the flow generated by a ring of stokeslets. Using the integral representation, it can be checked that all boundary conditions (2.23) are satisfied. We will number each basis function by its similarity exponent near the tip, i.e. $\Psi_\lambda = O(\rho^\lambda)$, where λ can be either an integer or a half-integer.

A key observation in the construction of three-dimensional solutions for the half-integer case, detailed in Appendix A, relies on the observation that the condition of vanishing shear stress for $\tilde{r} > 1$ can be replaced by the condition $V_r = \Psi_{\tilde{z}} = 0$; as a result, $E^4\Psi = 0$ factorizes into $E^2\Psi = \varphi$ (with conditions $\Psi = 0$ for $\tilde{r} < 1$ and $\Psi_{\tilde{z}} = 0$ for $\tilde{r} > 1$, at $\tilde{z} = 0$) and $E^2\varphi = 0$ (with conditions $\varphi = 0$ for $\tilde{r} < 1$ and $\varphi_{\tilde{z}} = 0$ for $\tilde{r} > 1$, at $\tilde{z} = 0$). In addition, the presence of mixed boundary conditions for Ψ makes more suitable to

write E^2 in oblate spheroidal coordinates (ξ, η), defined by $\tilde{z} + i\tilde{r} = \sinh(\xi + i\eta)$, and this enables us to find closed-form solutions. In the case of half-integer solutions, we find two sequences, one becoming increasingly singular (decreasing exponent), the other with increasing similarity exponent.

The first sequence has the form

$$\varphi_n = \frac{\lambda(1-\zeta^2)P_n(\lambda,\zeta)}{(\lambda^2+\zeta^2)^{2n-1}}, \quad E^2\psi_{\frac{5}{2}-n} = \varphi_n, \quad n \geqslant 1, \tag{2.27}$$

where P_n is a polynomial in two variables $\lambda = \sinh\xi$ and $\zeta = \cos\eta$; $\psi_{\frac{5}{2}-n}$ is then found through another two integrations. The asymptotic behavior of φ_n is

$$\varphi_n = O(\rho^{1/2-n}), \quad \varphi_n = \frac{C_n}{\tilde{r}},\ \tilde{r} \to \infty, \tag{2.28}$$

which is increasingly singular for increasing n.

The second sequence is of the form

$$\varphi_{-n} = G_n^{(-1/2)}(\zeta)H_n^{(-1/2)}(\lambda), \quad E^2\psi_{n+\frac{3}{2}} = \varphi_{-n}, \quad n \geqslant 1, \tag{2.29}$$

where the G_n are even Gegenbauer polynomials in ζ and $H_n^{(-1/2)}$ Gegenbauer functions of the second kind in λ. Now for $n \geqslant 1$

$$\varphi_{-n} = O(\rho^{n-1/2}), \quad \varphi_{-n} = C_n\tilde{r}^{2n},\ \tilde{r} \to \infty, \tag{2.30}$$

which means that all solutions (2.29) have velocities which grow at infinity. As a result, they cannot be matched to a static drop solution. Details of the basis functions of type (2.29) are given in Appendix A.

Next we come to integer solutions. Leaving the details to Appendix A, solutions with linear and quadratic local behaviors, and with finite velocities on the axis $\tilde{r} = 0$, are in cylindrical coordinates

$$\psi_1 = \tilde{r}^2\tilde{z}, \quad \psi_2 = \tilde{r}^4\tilde{z} - 4\tilde{r}^2\tilde{z}^3 - \tilde{r}^2\tilde{z}. \tag{2.31}$$

It can be checked that the local behavior of the integer solutions for small ρ is given by (2.24). All integer solutions have velocities which grow at least linearly at infinity, and thus again cannot be matched to a stationary outer solution.

We aim to write $\Psi(\tilde{r},\tilde{z})$ as a superposition of the basis functions ψ_λ, analogous to Brandão *et al.* (2026). Near $\tilde{r} = 1$, the second term of the left hand side of (2.21) behaves like $(\tilde{r}-1)^{-1/2}$, so Ψ can at most be as singular as $(\tilde{r}-1)^{1/2}$, which means that only functions from the first series (2.27) with $n \leqslant 2$ can contribute. As for the second series (2.29), all solutions correspond to unlimited growth of the velocity at infinity, and therefore cannot contribute. Thus, the only relevant solutions are $\psi_{\frac{1}{2}}$ and $\psi_{\frac{3}{2}}$, whose explicit form in oblate spheroidal coordinates is obtained from (2.27):

$$\psi_{\frac{1}{2}} = \frac{\lambda^3\left(1-\zeta^2\right)}{\lambda^2+\zeta^2}, \quad \psi_{\frac{3}{2}} = \left(1-\zeta^2\right)\left[\lambda - (1+\lambda^2)\mathrm{arctan}\lambda\right], \tag{2.32}$$

as highlighted already by Munro (2018). The pressures corresponding to (2.32) are found by integrating (4-15.5) of Happel & Brenner (1983); the result, for future reference, is

$$P_{\frac{1}{2}} = -2\zeta\frac{\lambda^4 + 3\lambda^2\left(1-\zeta^2\right) - \zeta^2}{\left(\lambda^2+\zeta^2\right)^3}, \quad P_{\frac{3}{2}} = -\frac{4\zeta}{\lambda^2+\zeta^2}. \tag{2.33}$$

In summary, on the bridge scale we can always write the streamfunction as a superposition

of the form

$$\Psi = A\psi_{\frac{1}{2}} + B\psi_{\frac{3}{2}}. \tag{2.34}$$

2.4. *The self-similar profile*

Equation (2.21) for the self-similar profile can be integrated as

$$W = \tilde{r}^2 \int_1^{\tilde{r}} \frac{\Psi_\rho(\rho, \tilde{z} = 0)}{\rho^4} d\rho. \tag{2.35}$$

We only need ψ_1, ψ_2 for $\tilde{z} = 0, \tilde{r} > 1$, in which case $\lambda = 0$ and $\zeta = \sqrt{\tilde{r}^2 - 1}$, and so

$$\psi_{\frac{1}{2}}(\tilde{r}, 0) = \sqrt{\tilde{r}^2 - 1}, \quad \psi_{\frac{3}{2}}(\tilde{r}, 0) = \sqrt{\tilde{r}^2 - 1} - \tilde{r}^2 \arctan\sqrt{\tilde{r}^2 - 1}. \tag{2.36}$$

Writing Ψ as the superposition (2.34), with A, B constant, we obtain $W = AW_{\frac{1}{2}} + BW_{\frac{3}{2}}$, with

$$W_{\frac{1}{2}} = \frac{1}{2}\left(\sqrt{\tilde{r}^2 - 1} + \arctan\sqrt{\tilde{r}^2 - 1}\right), \quad W_{\frac{3}{2}} = \left(1 - \frac{\tilde{r}^2}{2}\right)\arctan\sqrt{\tilde{r}^2 - 1} - \frac{\sqrt{\tilde{r}^2 - 1}}{2}. \tag{2.37}$$

Once we have identified the outer region on the scale of the drop, we are in a position to match all three regions.

2.5. *Drop scale and the Stokes limit*

The outer region is on the scale of the drops, which is unity, see Fig. 2. To leading order, the drops on the outer scale still have their static equilibrium shape, given by (2.1). The inner limit of this outer solution is

$$w = \frac{r^2}{2}, \tag{2.38}$$

to be compared to (2.2). Namely, the outer limits of the solutions (2.37) are

$$W_{\frac{1}{2}} \approx \frac{\pi\tilde{r}^2}{4}, \quad W_{\frac{3}{2}} \approx -\frac{\pi\tilde{r}^2}{4}, \quad \tilde{r} \to \infty, \tag{2.39}$$

and thus

$$w = r_0^2 W \approx r_0^2 \frac{r^2}{r_0^2}\left(A\frac{\pi}{4} - B\frac{\pi}{4}\right).$$

Comparing to (2.38), we obtain the condition

$$\frac{1}{2} = \frac{\pi}{4}(A - B), \tag{2.40}$$

which expresses matching to the drop.

On the other hand, matching the intermediate (bridge) region to the tip, we note that $W_{\frac{1}{2}} \approx \sqrt{2(\tilde{r} - 1)}$ for $\tilde{r} \to 1$, while by definition, $W_{\frac{3}{2}} \propto (\tilde{r} - 1)^{3/2}$, which is subdominant. Thus the inner limit of the intermediate solution behaves like $w \approx Ar_0^2\sqrt{2}(r/r_0 - 1)^{1/2}$. Now the interface of the tip solution according to (2.3) is

$$w = r_c\sqrt{2}\sqrt{\frac{r - r_0}{r_c}} = r_c^{1/2} r_0^{1/2}\sqrt{2}(r/r_0 - 1)^{1/2},$$

and so $Ar_0^{3/2} = r_c^{1/2}$, or

$$r_c = A^2 r_0^3. \tag{2.41}$$

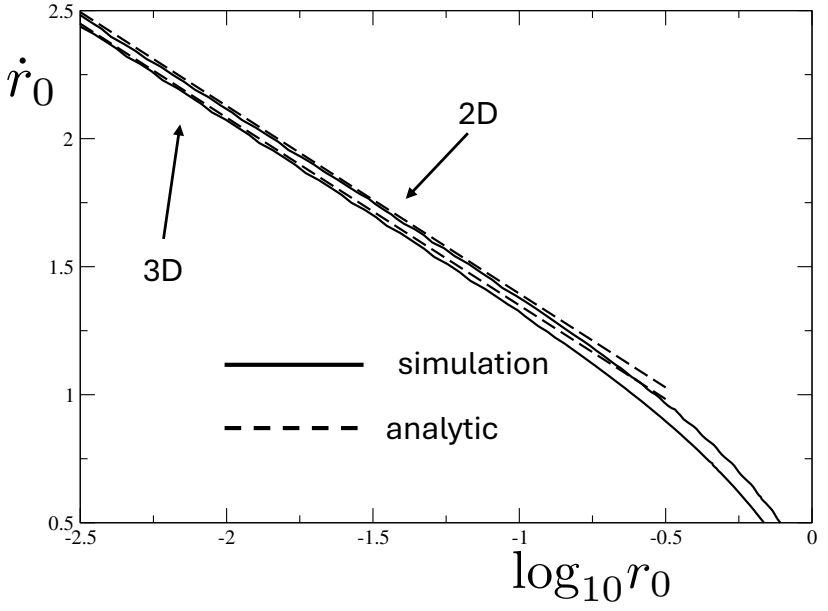

FIGURE 3. A comparison of full numerical simulations of inertialess coalescence (solid line) with asymptotic theory (dashed line) in both two and three dimensions. The dynamics of r_0 are compared to (2.46) and (2.45), which differ by a shift.

Finally, there is another condition associated with the fact that in Stokes flow, the force one drop exerts on the other must vanish exactly. To compute this force, we consider the far field of the solutions (2.32) at the intermediate (bridge) scale. In the limit $\tilde{r}^2+\tilde{z}^2 \to \infty$ they are

$$\psi_{\frac{1}{2}} = \frac{\tilde{r}^2}{(\tilde{z}^2+\tilde{r}^2)^{1/2}}, \quad \psi_{\frac{3}{2}} = -\frac{\pi\tilde{r}^2}{2} + \frac{2\tilde{r}^2}{(\tilde{z}^2+\tilde{r}^2)^{1/2}}; \tag{2.42}$$

the first contribution to $\psi_{\frac{3}{2}}$ corresponds to a constant velocity $v_z = \pi$. We will see that this results in a uniform translation of the drops, while keeping their shape. The leading contribution to $\psi_{\frac{1}{2}}$ and the second contribution to $\psi_{\frac{3}{2}}$ correspond to stokeslets of strength -8π and -16π, respectively, whose total contribution must vanish, to fulfill the requirement of a vanishing total force; this results in the condition $A + 2B = 0$. In the next section, we will recover the same relation in the limit $\mathrm{Oh} \to \infty$, when we formulate a more systematic calculation of the force exerted on one of the drops. Together with (2.40), this yields

$$A = \frac{4}{3\pi}, \quad B = -\frac{2}{3\pi} \tag{2.43}$$

for the Stokes limit.

2.6. *Results in two and three dimensions*

Using (2.43) and (2.41), we now have

$$r_c = \frac{16}{9\pi^2} r_0^3, \tag{2.44}$$

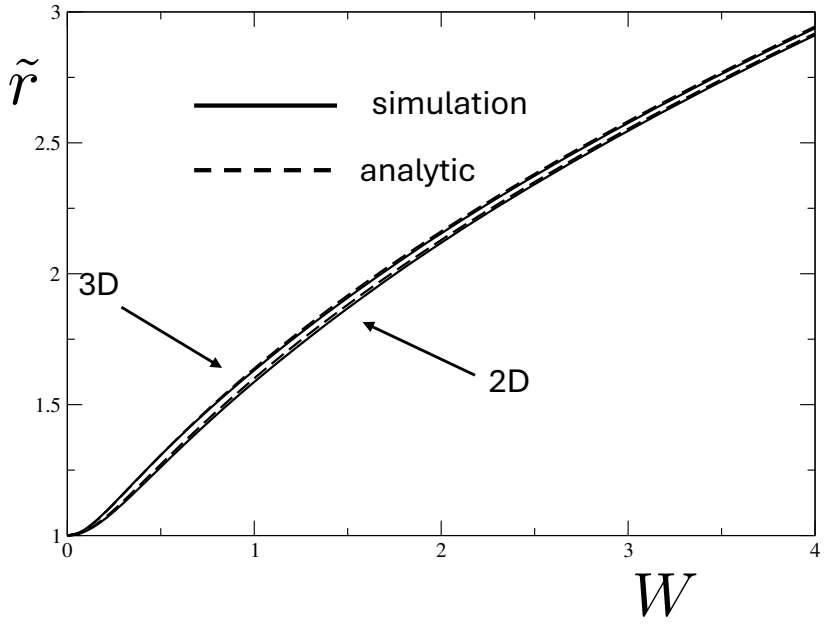

FIGURE 4. A comparison of the scaling function $W(\tilde{r})$, as defined by (2.2), between full numerical simulations (solid line) and asymptotic theory, as described by (2.49) and (2.48), for two and three dimensions, respectively. The numerical results for $W(\tilde{r})$ come from a rescaling of snapshots of the full profiles at $r_0 \approx 10^{-3}$.

which is a refinement of our previous estimate $r_c \sim r_0^3$. Inserting this into (2.13), we finally obtain the equation of motion for the bridge,

$$\dot{r}_0 \approx \frac{1}{\pi} \ln \frac{6\pi}{e r_0}, \tag{2.45}$$

which is represented in Fig. 3. This is to be compared to the two-dimensional result

$$\dot{r}_0 \approx \frac{1}{\pi} \ln \frac{8}{r_0}, \tag{2.46}$$

which follows from an analysis of Hopper (1990)'s solution. There is good agreement with theory as long as $r_0 \lesssim 10^{-1.5}$, while the difference between two and three dimensions is seen clearly.

Throughout this paper, we will be content with deriving an equation of motion of the form (2.45) or (2.46), from which $r_0(t)$ can be found by (numerical) integration. To leading order, both (2.45) and (2.46) yield

$$r_0(t) \approx -\frac{t}{\pi} \ln t, \tag{2.47}$$

as calculated in Eggers *et al.* (1999). However, we were not able to devise a convenient form of the trajectory $r_0(t)$ in terms of standard functions, which went beyond the leading asymptotics (2.47) to include the sub-leading terms contained in (2.45).

Next, superimposing $W_{\frac{1}{2}}$ and $W_{\frac{3}{2}}$, taken from (2.37), and using (2.43), we obtain the similarity profile

$$W = \frac{1}{\pi} \left[\arctan \sqrt{\tilde{r}^2 - 1} \left(\tilde{r}^2 - \frac{2}{3} \right) + \sqrt{\tilde{r}^2 - 1} \right], \tag{2.48}$$

to be compared to the two-dimensional result

$$W = \frac{\tilde{r}}{2}\sqrt{\tilde{r}^2 - 1}, \tag{2.49}$$

as shown in Fig. 4. To assure convergence, we have chosen a very early time, corresponding to $r_0 = 10^{-3}$, to compute the similarity profiles according to (2.2). The similarity profiles are also seen to agree well with numerical simulations, while there is a significant difference between two and three dimensions. Examining the asymptotics of W for large $\tilde{r}$, one finds $W \approx \tilde{r}^2/2 - 1/4$ and $W \approx \tilde{r}^2/2 - 1/3$, in two and three dimensions, respectively. Thus in real space, the extrapolated end z_s of the right drop is at

$$z_s = -\frac{r_0^2}{4}\ (2\mathrm{D}), \quad z_s = -\frac{r_0^2}{3}\ (3\mathrm{D}), \tag{2.50}$$

which implies a translational motion of the drops in the viscous limit. However, if Oh is finite, inertial effects have to be taken into account, which inhibits this translational motion, as pointed out by Paulsen *et al.* (2012). In the next section, we will study the effect of this translational motion more systematically.

3. Inertial corrections

3.1. *Force balance*

To account for inertia, we balance the total force exerted on one drop via the neck with the translational inertia of the drop. Using the Reynolds transport theorem on (1.1) as well as the divergence theorem, we obtain

$$\frac{1}{\mathrm{Oh}^2}\frac{d}{dt}\int_{\mathcal{D}(t)} \mathbf{v} d^3x = \int_{\mathcal{D}(t)} \boldsymbol{\nabla}\cdot\boldsymbol{\sigma} d^3x = -\int_{\mathcal{C}_0(t)} \mathbf{e}_z\cdot\boldsymbol{\sigma} ds - \int_{\mathcal{S}_d(t)} \mathbf{n}\cdot\boldsymbol{\sigma} ds, \tag{3.1}$$

where $\mathcal{D}(t)$ is the domain of the drop with $z > 0$, $\mathcal{C}_0(t)$ is the cross section of the neck, and $\mathcal{S}_d = \partial\mathcal{D} \setminus \mathcal{C}_0$ the free surface of the drop. Using the boundary condition (1.2) on the last integral of (3.1) and manipulating the resulting surface integral as in Eggers & Fontelos (2005), we arrive at the force balance

$$\frac{1}{\mathrm{Oh}^2}\frac{d}{dt}\int_{\mathcal{D}(t)} v_z d^3x = -\int_{\mathcal{C}_0(t)} \sigma_{zz} ds - 2\pi r_0(t). \tag{3.2}$$

The two terms on the right hand side of (3.2) represent the total force on the drop, coming from the total stress over the neck surface and from surface tension, respectively. In Paulsen *et al.* (2012), only the surface tension term was considered. We will see below that the stress term is equally important, and cancels out surface tension to leading order as $r_0 \to 0$, making the total force $\propto r_0^2$ instead of $\propto r_0$.

We first calculate the integral on the left of (3.2), which comes from the translational motion of the drop. Indeed, the leading order contribution to (2.18) in the far field comes from the first term of $\psi_{\frac{3}{2}}$ in (2.42), which results in a constant velocity $v_z = \pi B r_0 \dot{r}_0$. Integrating that over the volume of a spherical drop we obtain

$$\int_{\mathcal{D}(t)} v_z d^3x \approx \frac{4B\pi^2}{3} r_0 \dot{r}_0. \tag{3.3}$$

On the other hand, the far field contribution from ψ_{Stokes} in (2.18) vanishes when averaged in the radial direction. In the bridge region, the velocity is $O(1)$, but the volume is $O(r_0^3)$, and thus its contribution is negligible.

Next, to calculate the integral on the right of (3.2), we separate out a narrow rim

of width ϵ from around the meniscus, in order to account for the singular contribution coming from the tip of size r_0^3:

$$\int_{\mathcal{C}_0(t)} \sigma_{zz} ds = 2\pi \int_0^{r_0-\epsilon} \sigma_{zz} r dr + 2\pi \int_{r_0-\epsilon}^{r_0} \sigma_{zz} r dr, \tag{3.4}$$

with $r_c \ll \epsilon \ll r_0$. Evaluating the second integral of (3.4), since the rim is much narrower than r_0, the flow can be considered as two-dimensional, and corresponds to Hopper's parabolic solution (2.6). In this representation, the normal stress on an arbitrary boundary can be written as (Crowdy & Tanveer 1998)

$$\mathbf{n} \cdot \boldsymbol{\sigma} = 2i \frac{dH}{ds}, \tag{3.5}$$

where s is the arclength along the boundary, and

$$H = g(z) + z\overline{g'(z)} + \overline{f'(z)}. \tag{3.6}$$

Here the x- and y-components of $\mathbf{n} \cdot \boldsymbol{\sigma}$ are understood as the real and imaginary parts of a complex expression, respectively. Now the integrated stress over the boundary is given by the difference in H between the end points, which we can write as $\zeta = i\sqrt{\epsilon/(2r_c)}$ and $\zeta = 0$ in the mapping of (2.4). Explicitly, putting $\zeta = i\xi/2$, $H(\xi)$ is

$$H(\xi) = \frac{\xi + (\xi^2 - \xi - 1)\mathrm{arccosh}(\xi)/\sqrt{\xi^2 - 1}}{(\xi^2 - 1)\pi}. \tag{3.7}$$

Thus in the limit of $r_0 \to 0$, transforming to tip scale variables (cf. (2.3), where Σ_{zz} refers to the dimensionless version of the corresponding stress component)

$$\int_{r_0-\epsilon}^{r_0} \sigma_{zz} r dr \approx r_0 \int_{-\epsilon/r_c}^{0} \Sigma_{zz} dX = 2r_0 \left(H(\sqrt{2\epsilon/r_c}) - H(0) \right). \tag{3.8}$$

Now $H(0) = 1/2$, while for large ξ

$$H(\xi) = \frac{1}{\pi\xi} \ln(2e\xi) + O(\xi^{-2} \ln \xi). \tag{3.9}$$

Thus the leading contribution to the second integral on the right of (3.4) is $-2\pi r_0$, which cancels the contribution from surface tension on the right of (3.2). As a result, we have to go to the next order in calculating (3.4), which comes from the logarithm in (3.9). Using (2.41) and (2.13), (3.9) can be estimated as

$$H(\xi) \approx \frac{\ln 2e\xi}{\pi\xi} \approx \frac{Ar_0}{2\pi} \sqrt{\frac{r_0}{2\epsilon}} \ln \frac{8e^2\epsilon}{r_c} \approx Ar_0\dot{r}_0 \sqrt{\frac{r_0}{2\epsilon}} \frac{\ln \frac{8e^2\epsilon}{r_c}}{\ln \frac{64r_0}{e^2 r_c}} \approx Ar_0\dot{r}_0 \sqrt{\frac{r_0}{2\epsilon}} \left(1 + \frac{\ln \frac{e^4\epsilon}{8r_0}}{\ln \frac{64}{e^2 A^2 r_0^2}} \right).$$

Now we choose $\epsilon = r_0/|\ln r_0| \ll r_0$, so that the contribution to the second integral in (3.4) becomes

$$2Ar_0\dot{r}_0 \left(\sqrt{\frac{r_0}{2\epsilon}} + O\left(\frac{\ln(\ln r_0)}{|\ln r_0|^{1/2}} \right) \right), \tag{3.10}$$

with a correction in brackets which goes to zero as $r_0 \to 0$. In calculating the first integral on the right of (3.4) we expect (3.10) to cancel, since the end result (3.4) of course has to be independent of ϵ.

To evaluate the first integral, we find σ_{zz} in terms of the two solutions (2.32) on the bridge scale, whose pressure distributions are given by (2.33). We only need the stress for $z = 0$, such that $\xi = \lambda = 0$, and $\zeta = \sqrt{1 - r^2}$. Since both $\psi_{\frac{1}{2}}$ and $\psi_{\frac{3}{2}}$ behave like λ^3

for $\lambda \to 0$, the deviatoric stress contributions vanish exactly for $z = 0$, and we only have to consider the pressure, which from (2.33) becomes

$$P_{\frac{1}{2}} = \frac{2}{(1-\tilde{r}^2)^{3/2}}, \quad P_{\frac{3}{2}} = -\frac{4}{(1-\tilde{r}^2)^{1/2}}.$$

The integrals can be performed trivially, and rewriting them in bridge scale variables as defined by (2.18) yields

$$\int_0^{r_0-\epsilon} \sigma_{zz} r dr = -r_0^2 \dot{r}_0 \int_0^{1-\epsilon/r_0} P \tilde{r} d\tilde{r} = r_0^2 \dot{r}_0 \left[2A + 4B - A\sqrt{\frac{2r_0}{\epsilon}} - 4B\sqrt{\frac{2\epsilon}{r_0}} \right].$$

The third term in square brackets indeed cancels exactly against (3.10) above, while the fourth term vanishes for $\epsilon \to 0$. In summary, the total force (3.4) becomes

$$\int_{\mathcal{C}_0(t)} \sigma_{zz} ds \approx 4\pi r_0^2 \dot{r}_0 (A + 2B), \tag{3.11}$$

so that to leading order, (3.2) becomes

$$\frac{1}{\mathrm{Oh}^2} \frac{d}{dt} \left(B r_0 \dot{r}_0 \right) = -\frac{3}{\pi} \left(A + 2B \right) r_0^2 \dot{r}_0. \tag{3.12}$$

In the limit of large Oh, we find $A + 2B = 0$, as deduced before in the Stokes limit. On the other hand, for very early times inertia dominates and we have $B = 0$. In both limiting cases the coefficients are constants. In general, however, the coefficients A and B are now time-dependent, and we compute this time dependence next.

3.2. *Amplitude equation*

In order to find the time dependence of the two amplitudes $A(t)$ and $B(t)$, we need another relation between the two in addition to (3.12). To that end we solve the kinematic equation (2.17) in which the second term on the left is subdominant. Hence in view of (2.20) and (2.22), using the superposition (2.34):

$$\frac{\partial w}{\partial t} = -\frac{A(t)}{r} \frac{\partial \psi_{\frac{1}{2}}}{\partial r} - \frac{B(t)}{r} \frac{\partial \psi_{\frac{3}{2}}}{\partial r} = r_0 \dot{r}_0 \left(-\frac{A(t)}{\sqrt{(r/r_0)^2 - 1}} + 2B(t) \arctan \sqrt{(r/r_0)^2 - 1} \right). \tag{3.13}$$

The initial condition (2.1) corresponds to $w(r, t = 0) = r^2/2$. In contrast to the viscous case of the previous section, the amplitudes A and B are now time-dependent, and we must integrate the kinematic condition in time, since W in (2.2) is not longer time-independent. Integrating (3.13) in time, we obtain

$$w(r,t) = \frac{r^2}{2} + \int_0^t \left(-\frac{A(t')}{\sqrt{(r/r_0)^2 - 1}} + 2B(t') \arctan \sqrt{(r/r_0)^2 - 1} \right) r_0 \dot{r}_0 dt',$$

and since $w(r_0, t) = 0$, we arrive at the condition

$$\frac{r_0^2}{2} = \int_0^t \left(\frac{\omega A(t')}{\sqrt{(r/r_0)^2 - 1}} - 2B(t') \arctan \sqrt{(r/r_0)^2 - 1} \right) r_0 \dot{r}_0, dt',$$

which using the transformation $\omega = r_0(t')$ can be written as

$$\frac{r_0^2}{2} = \int_0^{r_0} \frac{A(\omega)\omega}{\sqrt{(r_0/\omega)^2 - 1}} d\omega - \int_0^{r_0} 2\omega B(\omega) \arctan \sqrt{(r_0/\omega)^2 - 1} d\omega. \tag{3.14}$$

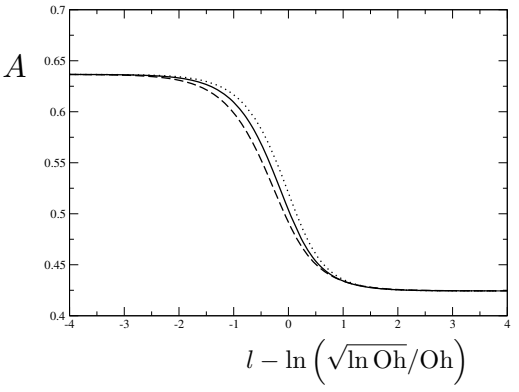

FIGURE 5. The amplitude A as a function of $l = \ln r_0$, but shifted as suggested by the definition of σ, for $\mathrm{Oh} = 10$ (dotted line) and $\mathrm{Oh} = 100$ (solid line). The dashed line is the universal profile (3.23).

Integrating the second integral in (3.14) by parts, and putting $\bar{A} = A - 2/\pi$, (3.14) becomes

$$\int_0^{r_0} \frac{1}{\sqrt{(r_0/\omega)^2 - 1}} \left[\omega \bar{A}(\omega) - \frac{2}{\omega} \int_0^{\omega} \omega' B(\omega' d\omega')\right] d\omega = 0.$$

Since this is true for general r_0, the expression in square brackets must vanish, i.e.

$$r_0^2 \bar{A}(r_0) - 2 \int_0^{r_0} \omega' B(\omega') d\omega' = 0.$$

Differentiating with respect to r_0, we obtain in terms of the original variable A:

$$\frac{dA}{dr_0} = \frac{2}{r_0} \left(B(r_0) - A(r_0) + \frac{2}{\pi}\right), \tag{3.15}$$

which must be solved together with the force balance (3.16).

To achieve this, we replace time as the independent variable in (3.16) by a parametric dependence on r_0, using $\dfrac{d}{dt} = \dot{r}_0 \dfrac{d}{dr_0}$. Also, for convenience, we introduce $r_s = \sqrt{r_c/r_0}$, so that $A = r_s/r_0$. Then from (3.12) we find

$$\frac{d}{dr_0} \left(B r_0 \dot{r}_0\right) = -\frac{3}{\pi} \left(A + 2B\right) r_0^2 \mathrm{Oh}^2, \tag{3.16}$$

where

$$\dot{r}_0 = \frac{1}{\pi} \ln \frac{8}{e r_s} = \frac{1}{\pi} \ln \frac{8}{e A r_0} \tag{3.17}$$

can be used to eliminate $\dot{r}_0$ in favor of r_s or A. Then (3.15) and (3.16) become a system of equations for $A(r_0), B(r_0)$. To find $A(r_0)$ numerically, it is advantageous to switch to the logarithmic variable $l = \ln r_0$, so that the system for the amplitudes A, B becomes

$$\frac{dA}{dl} = 2B - 2A + \frac{4}{\pi}, \tag{3.18}$$

$$\frac{dB}{dl} = \left[-3(A + 2B) e^{2l} \mathrm{Oh}^2 + B \left(1 - \ln \frac{8}{e A e^l}\right)\right] \left(\ln \frac{8}{e A e^l}\right)^{-1}. \tag{3.19}$$

For large and negative l, the initial condition is $A = 2/\pi$, $B = 0$, while for large and positive l one reaches the Stokes limit (2.43), for which $A = 4/(3\pi)$ and $B = -2/(3\pi)$.

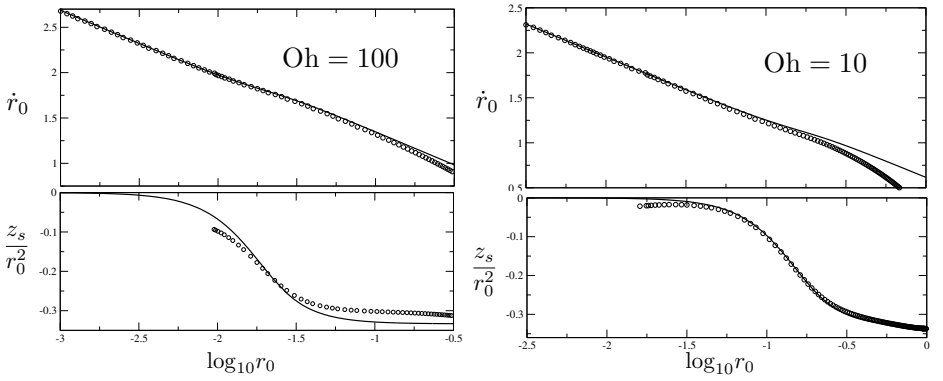

FIGURE 6. The radial tip speed $\dot{r}_0$ (top) and the relative shift of the droplets z_s/r_0^2 (bottom) as a function of of $\log_{10} r_0$, for Oh = 100 (left) and Oh = 10 (right). The solid lines are the theory, as found from (3.17) for $\dot{r}_0$ and from (3.27) below; A is found solving the system (3.18),(3.19). The symbols are the results of our numerical simulations described in subsection 1.1.

Instead of integrating (3.18),(3.19) numerically, we can find an analytical solution in the limit of large Oh. To that end, we rescale the independent variable according to $\sigma = r_0 \dfrac{\mathrm{Oh}}{\sqrt{\ln \mathrm{Oh}}}$; then from (3.15) we find

$$\frac{d(\sigma^2 A)}{d\sigma} = 2\sigma B + \frac{4\sigma}{\pi}. \tag{3.20}$$

Moreover, noting that

$$\dot{r}_0 = \frac{1}{\pi}\ln\frac{8}{eA} - \frac{1}{\pi}\ln r_0 = \frac{1}{\pi}\left(\ln\frac{8}{eA} - \ln\sigma + \ln \mathrm{Oh} - \frac{1}{2}\ln(\ln \mathrm{Oh})\right) \approx \frac{1}{\pi}\ln \mathrm{Oh},$$

the force balance (3.16) simplifies to

$$\frac{d(B\sigma)}{d\sigma} = -3(A+2B)\sigma^2. \tag{3.21}$$

The two equations (3.20) and (3.21) can be combined into a single equation for $\bar{A} = A - 2/\pi$:

$$\frac{d^2(\sigma^2\bar{A})}{d\sigma^2} + 6\frac{d(\sigma^2\bar{A})}{d\sigma} = -6\sigma^2\bar{A} - \frac{12\sigma^2}{\pi}. \tag{3.22}$$

The unique solution of (3.22) which is finite for $\sigma \to 0$ is

$$\bar{A} = -\frac{2}{3\pi} + \frac{2}{9\pi\sigma^2}\left(1 - e^{-3\sigma^2}\right). \tag{3.23}$$

From (3.27) one recovers that for early times ($\sigma \to 0$) $\bar{A} = 0$, while for late times $\bar{A} = -2/(3\pi)$. The universal profile (3.23) is plotted as the dashed line in Fig. 5, and compared to the numerical solution of the full system (3.18),(3.19) for Oh = 10 and 100. There is good collapse of the two numerical profiles, and good agreement with the shape of the limiting universal profile for large Oh. As for the shift, the convergence onto the limiting profile is however slow, and we will use the numerical solutions to describe the crossover between the two regimes.

We are now in a position to compute, for a given Oh, the meniscus speed $\dot{r}_0$ as a function of $\log_{10} r_0$, as seen on the top of Fig. 6 for Oh = 100 (left) and Oh = 10 (right). To compute $\dot{r}_0$, we use (3.17), for which we need $A(r_0)$ as well. To this end we compute

$A(l = \ln r_0)$ from integrating the system (3.18),(3.19), which contains Oh as a parameter. The circles are the data from corresponding full numerical simulations, as described in Subsect. 1.1. For small r_0, the numerics agree very well with the predicted linear dependence

$$\dot{r}_0 = \frac{1}{\pi}\ln\frac{4\pi}{e} - \frac{\ln 10}{\pi}\log_{10} r_0,$$

which crosses over to

$$\dot{r}_0 = \frac{1}{\pi}\ln\frac{6\pi}{e} - \frac{\ln 10}{\pi}\log_{10} r_0$$

for late times. The corresponding shift is visible clearly for Oh = 100, but for Oh = 10 is masked by corrections coming from the fact that r_0 is no longer small compared to the drop radius 1, and therefore our asymptotic theory no longer applies.

To clarify this, and to illustrate the intimate connection between the scaling of $\dot{r}_0$ and the inertia-limited motion of the drops, we also plot the position of the drops z_s relative to their initial values at the bottom of Fig. 6. This shift is simplest to compute on the basis of the entire gap profile, which we calculate in the next subsection; the result is given in (3.27). As expected, the shift is of the order of the gap width, so we normalize the result dividing by r_0^2. This makes our numerical results very sensitive to errors in the drop positions, which are computed on a much coarser grid then the gap region. To mitigate this fact, the numerical calculation of z_s was based on the center of mass of the drops, to cancel out errors. As seen in Fig. 6, our numerics captures the position of the crossover very well, and in the case of Oh = 10 in particular, the shape of the crossover profile calculated theoretically. We do not report numerical results for $r_0 < 0.01$ in the case of Oh = 100, and $r_0 < 0.018$ in the case of Oh = 10, because round-off errors become prohibitively large.

3.3. *Gap profile*

The gap profile $w(r,t)$ can again be found from the kinematic equation (3.13), given in terms of a superposition of modes $\psi_{\frac{1}{2}}$ and $\psi_{\frac{3}{2}}$. For early times, $B = 0$ and $A = 2/\pi$, so separating w into the profile $w = r_0^2 W_{\frac{1}{2}}$ for early times, and a remainder $\bar{w}$, we have

$$w(r,t) = \frac{r_0^2}{\pi}\left(\sqrt{\tilde{r}^2-1} + \arctan\sqrt{\tilde{r}^2-1}\right) + \bar{w}(r,t), \tag{3.24}$$

where

$$\frac{\partial \bar{w}}{\partial t} = \frac{\bar{A} r_0 \dot{r}_0}{\sqrt{\tilde{r}^2-1}} + 2B r_0 \dot{r}_0 \arctan\sqrt{\tilde{r}^2-1} = \left(\bar{A} r_0^2 \dot{r}_0 \frac{d}{dr_0} + 2B r_0 \dot{r}_0\right)\arctan\sqrt{\tilde{r}^2-1}.$$

Using (3.15) or $\dfrac{d(r_0^2\bar{A})}{dr_0} = 2r_0 B$, we obtain

$$\frac{\partial \bar{w}}{\partial t} = \dot{r}_0 \frac{d}{dr_0}\left(\bar{A} r_0^2 \arctan\sqrt{\tilde{r}^2-1}\right) = \frac{d}{dt}\left(\bar{A} r_0^2 \arctan\sqrt{\tilde{r}^2-1}\right).$$

We can now integrate to find

$$\bar{w} = \bar{A} r_0^2 \arctan\sqrt{\tilde{r}^2-1} + G(\tilde{r}), \tag{3.25}$$

and using (3.24), we conclude that in the limit $r_0 \to 0$ (since $\bar{A} = A - 2/\pi \to 0$), we obtain

$$w(r,t) = \frac{r^2}{2} + G(\tilde{r}), \quad r_0 \to 0.$$

Comparing to the initial condition $w(r,0) = r^2/2$ this implies $G(\tilde{r}) = 0$, so finally the thickness profile in the bridge region is $w = r_0^2 W(\tilde{r}, t)$, with

$$W(\tilde{r}, t) = \frac{\sqrt{\tilde{r}^2 - 1}}{\pi} + \frac{\tilde{r}^2}{\pi} \arctan\sqrt{\tilde{r}^2 - 1} + \bar{A} \arctan\sqrt{\tilde{r}^2 - 1}. \tag{3.26}$$

This result gives the gap thickness profile for any given time t. It is no longer a similarity solution, in that the rescaled profile W itself depends on time through $\bar{A}$. However, in the limits of early times ($\bar{A} = 0$), and late times ($\bar{A} = -2/(3\pi)$), similarity solutions are recovered. An example of a profile in the transition region between early and late times is shown in Fig 7, and compared to numerical simulations. In the main panel, we compare a rescaled numerical profile at $\mathrm{Oh} = 100$ and $r_0 = 0.0123$ (solid line) to the theoretical prediction (3.26) with $\bar{A} = 0.5746$ (dashed line), which comes from integrating (3.18),(3.19). Almost perfect agreement is found over a wide range of the rescaled variable, as shown in the main panel as well as the inset, showing a close-up of the tip region.

The inclusion of inertial effects is key to reach this level of agreement. This is demonstrated by the fact that the profile which is calculated on the basis of the Stokes equation alone (the dot dashed line in the inset), lies far off the true profile. The formula (3.26) also reveals a remarkable symmetry of the coalescence problem, in that there is only a single parameter $\bar{A}$ appearing in it. This means the profile for a different value of Oh, but with r_0 chosen such that $\bar{A}$ is the same, will have an identical profile. This prediction is checked as well in Fig. 7, by plotting the rescaled profile for $\mathrm{Oh} = 10$ and $r_0 = 0.1$ obtained from numerical simulations, as the dotted line in the inset. The very close agreement between the two numerical curves (the solid and dotted lines), which both correspond to the same value $\bar{A} = 0.5746$, confirms this theoretical prediction. This agreement is best seen in a smaller region around the tip (as shown in the inset), since $r_0 = 0.1$ is not small enough for the numerical profile to have converged onto a self-similar profile on the scale of the entire window shown in Fig. 7.

As a corollary to (3.26), we can infer the shift of the drops, which move toward one another virtually without deformation, except in the bridge region. Namely, analyzing (3.26) for large $\tilde{r}$, we find $W \approx \tilde{r}^2/2 + \pi\bar{A}/2$. Thus the drop shift is

$$z_s = \frac{\pi \bar{A}}{2} r_0^2, \tag{3.27}$$

which we have compared to numerical simulations in Fig. 6. At early times (small r_0), the shift vanishes, and eventually crosses over to its maxmum value for purely viscous drops.

4. Discussion

In Fig. 8 we compare the predictions of our theory to experimental data of drop shapes for $\mathrm{Oh} = 370$ (left) and for $\mathrm{Oh} = 0.62$ (right), taken from Paulsen (2013). The results of our theory are always shown on the right hand side of each (symmetric) profile, the left hand side is reserved for comparison with full numerical simulations of the Navier-Stokes equation. On account of the transition taking place around $r_0 \propto 1/\mathrm{Oh}$, we predict that inertia plays no role for $\mathrm{Oh} = 370$, while inertia arrests translation of the drops As a result, our prediction for the profiles on the left is (3.26) with $\bar{A} = -2/(3\pi)$ (black dashed lines). This works well until with increasing r_0 the agreement fails in the data of drop shapes for $\mathrm{Oh} = 370$ (left) and for $\mathrm{Oh} = 0.62$ (right), taken from Paulsen (2013). On account of the transition taking place around $r_0 \propto 1/\mathrm{Oh}$, we predict that inertia plays no

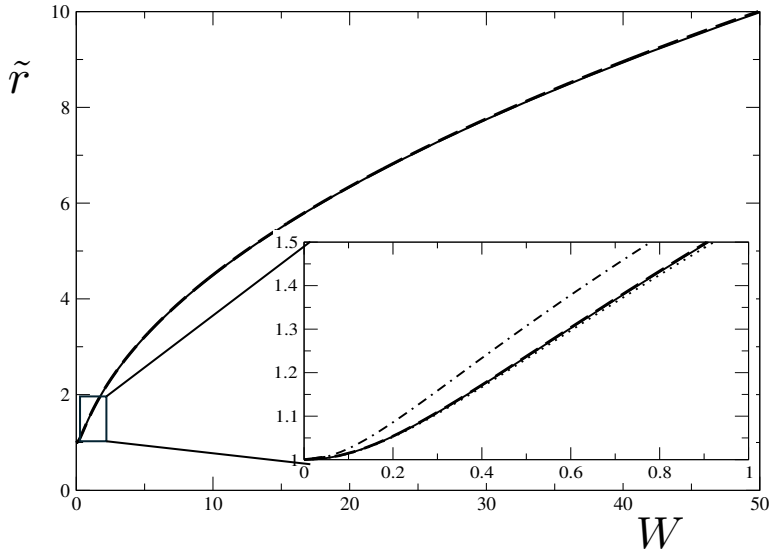

FIGURE 7. Comparison of the theoretical bridge profile (3.26) (dashed line) with a numerical simulation of drop coalescence (solid line). The numerical profile has been rescaled according to $w = r_0^2 W(\tilde{r})$, and taken at Oh = 100 and $r_0 = 0.0123$. From this, we obtain $\bar{A} = -0.06202$ in (3.26). In the inset, the dotted line is the rescaled numerical profile for Oh = 10 and $r_0 = 0.1$, for which $\bar{A}$ has the same value, so that the two numerical profiles collapse. The purely viscous prediction (2.48) is shown as the dot-dashed line for comparison.

role for Oh = 370, while inertia arrests translation of the drops for Oh = 0.62. As a result, our prediction for the profiles on the left is (3.26) with $\bar{A} = -2/(3\pi)$ (black dashed lines). This works well until with increasing r_0 the agreement fails in the wings of the profiles, as our assumption of asymptotically small r_0 is no longer satisfied. This is confirmed by the good agreement with a full numerical simulation on the left of each profile (black solid lines), demonstrating that all the modeling assumptions of our calculation are satisfied, the only shortcoming of theory being that it does not work for values of r_0 which have become comparable to unity. The fact that all inertial effects were neglected in the simulation (Oh $= \infty$) does not affect the comparison, because for Oh = 370 inertial effects are uniformly small.

On the other hand, on the right of Fig. 8 (Oh = 0.62), we predict that inertia dominates the translational motion of the drops, which means that we now put $\bar{A} = 0$ in the theoretical prediction (3.26) for the similarity profile (colored dashed lines on the right of the profiles). The agreement is good for the smallest r_0, significantly better than the agreement with the black dashed line, which is the result for Stokes flow (drop inertia neglected, putting $\bar{A} = -2/(3\pi)$ in (3.26)). This trend continues as r_0 increases, but there are significant deviations owing to r_0 no longer being small, so our asymptotic theory applies less and less. This is seen once more comparing to the solid lines on the left of each profile, showing full numerical simulations of the Navier-Stokes equation at Oh = 1. Although the Ohnesorge number used for the simulation does not perfectly match the value of the experiment is not a concern, since for Oh = 1 we are still in the regime of inertially dominated drop motion.

Let us highlight once more that while Paulsen *et al.* (2012) first raised the possibility of translational inertia playing a role in the early stages of drop coalescence, they claimed a crossover for (neglecting logarithmic corrections) $r_0 \approx 1/\mathrm{Oh}^2$, while we show that a

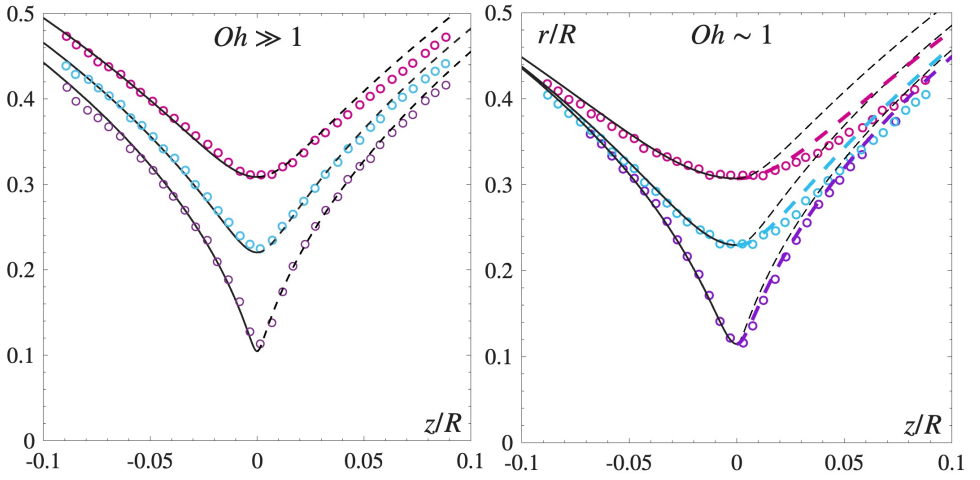

FIGURE 8. Comparison of experimental neck shapes (symbols, from Paulsen (2013)) to theory for Oh = 370 (left) and Oh = 0.62 (right). All theoretical data have been fitted to match the experimental values of r_0. The black solid lines on the left half of each profile are the results of full numerical calculations of the Navier-Stokes equation (see Sprittles & Shikhmurzaev (2014)), for Oh = ∞ (left), and Oh = 1 (right). The right half of each profile presents a comparison with our theory. On the left, we compare to (3.26) with $\bar{A} = -2/(3\pi)$ (black dashed lines), representing viscously dominated drop motion. On the right, we compare to (3.26) with $\bar{A} = 0$ (colored dashed lines), representing inertially dominated drop motion. For comparison, on the right of each profile we also show the Stokes flow prediction ($\bar{A} = -2/(3\pi)$) as the black dashed lines.

crossover takes place for $r_0 \approx 1/\mathrm{Oh}$ instead. This fact does not change the leading-order logarithmic correction to the meniscus speed $\dot{r}_0$, which was predicted by the viscous theory of Eggers *et al.* (1999). Instead, inertia is felt in the sub-leading terms of the dynamics of r_0, which we compute. Concomitant with these corrections, the gap profile between the drops varies with time on the scale of the gap width r_0^2, to accommodate the inertia-dependent position of the two drops' centers of mass. This is a novel effect which shows how a similarity description can in part be controlled by boundary conditions. This contrasts with e.g. the case of drop breakup Eggers (1993), for which the self-similar breakup profile is universal, regardless of boundary conditions.

Declaration of Interests. The authors report no conflict of interest.

Acknowledgments

R. B. acknowledges funding from the NSERC (Discovery Grant RGPIN-2026-06977); M. A. F. acknowledges financial support through project TED2021-131530B-I00; J. E. S. would like to acknowledge funding from the EPSRC (grant reference UKRI3193). We are grateful to Luke Neville for inspiring discussions.

Appendix A. Basis functions for the double-slit domain

In this appendix, we provide details for the stream functions $\psi_\lambda \propto \rho^\lambda$, valid on the bridge scale, satisfying boundary conditions (2.23). Focusing on the case $\lambda > 0$, which is

the physically relevant one, the similarity exponent λ can be either integer or half-integer, see (2.24), (2.25). For ease of notation, we omit the tildes on top of the independent variables. Note that $(r < 1, z = 0)$ corresponds to $(\lambda = 0, 0 < \zeta < 1)$ in oblate spheroidal coordinates, and $(r > 1, z = 0)$ to $(\lambda > 0, \zeta = 1)$.

The Half-Integer Case

The boundary conditions are $\psi_z = 0$ and $\varphi_z = 0$ for $(r > 1, z = 0)$, which we write as $\psi_\eta = \sqrt{1-\zeta^2}\psi_\zeta = 0$ and $\varphi_\eta = \sqrt{1-\zeta^2}\varphi_\zeta = 0$ for $(\lambda > 0, \zeta = 1)$. On the interval $(\lambda = 0, 0 < \zeta < 1)$, we impose that both ψ and φ vanish.

In the first series of solutions, we write

$$E^2\psi_{\frac{5}{2}-n} = \varphi_n, \quad n = 1, 2, \ldots. \tag{A 1}$$

We choose $\varphi_n(\lambda, \zeta)$ such that $\varphi_n = 0$ at $(\lambda = 0, 0 < \zeta < 1)$ and $\varphi_{n,\eta} = \sqrt{1-\zeta^2}\varphi_{n,\zeta} = 0$ for $(\lambda > 0, \zeta = 1)$ by writing

$$\varphi_n = \frac{\lambda(1-\zeta^2)P_n(\lambda, \zeta)}{(\lambda^2+\zeta^2)^{2n-1}}, \tag{A 2}$$

and searching for a polynomial $P_n(\lambda, \zeta)$ that provides a solution to $E^2\varphi_n = 0$. The first three solutions are:

- $n = 1, \quad P_1(\lambda, \zeta) = 1$
- $n = 2, \quad P_2(\lambda, \zeta) = \lambda^2 - 3\zeta^2 - 3\zeta^2\lambda^2 + \lambda^4$
- $n = 3, \quad P_3(\lambda, \zeta) = \lambda^4 + 5\zeta^4 - 10\zeta^2\lambda^2 + 3\lambda^6 - 7\zeta^6 + 5\zeta^4\lambda^2 - 17\zeta^2\lambda^4 + \frac{7}{4}\zeta^8 + \frac{21}{2}\zeta^4\lambda^4 + \frac{15}{4}\lambda^8$.

Cases where $n \geqslant 3$ provide solutions too singular to be physically relevant.

Next, we consider the second series of solutions:

$$E^2\psi_{n+\frac{3}{2}} = \varphi_{-n}, \quad n = 1, 2, \ldots, \tag{A 3}$$

where $E^2\varphi_{-n} = 0$. By expressing E^2 in oblate spheroidal coordinates, we arrive at:

$$\left(\frac{\lambda^2+1}{\lambda^2+\zeta^2}\frac{\partial^2}{\partial\lambda^2} + \frac{1-\zeta^2}{\lambda^2+\zeta^2}\frac{\partial^2}{\partial\zeta^2}\right)\varphi_{-n} = 0. \tag{A 4}$$

A standard separation-of-variables technique leads to

$$\varphi_{-n} = G_n^{(-1/2)}(\zeta)H_n^{(-1/2)}(\lambda), \tag{A 5}$$

where $G_n^{(-1/2)}(\zeta)$ is an even Gegenbauer polynomial in ζ and $H_n^{(-1/2)}(\lambda)$ is a second-kind Gegenbauer function in λ. In order to satisfy the boundary conditions, we search for Gegenbauer polynomials and functions that are even in ζ and odd in λ, respectively:

$$\begin{aligned} G_1^{(-1/2)}(\zeta) &= (1-\zeta^2), \\ G_2^{(-1/2)}(\zeta) &= (1-\zeta^2)\left(1-\frac{1}{5}\zeta^2\right), \\ &\vdots \end{aligned} \tag{A 6}$$

and

$$\begin{aligned} H_1^{(-1/2)}(\lambda) &= (1+\lambda^2)\arctan\lambda + \lambda, \\ H_2^{(-1/2)}(\lambda) &= (1+6\lambda^2+5\lambda^4)\arctan\lambda + \frac{13}{3}\lambda + 5\lambda^3. \end{aligned} \tag{A 7}$$

In the general case one can write

$$H_m^{(-1/2)}(\lambda) = P_{2m}(\lambda)\arctan\lambda + \lambda Q_{2m-2}(\lambda), \tag{A 8}$$

with suitable polynomials $P_{2m}(\lambda)$ and $Q_{2m-2}(\lambda)$, whose detailed form will not be pursued here. Once the corresponding functions φ_n and φ_{-n} have been found, we compute the stream functions by solving (A 1) and (A 3) under the established boundary conditions.

The Integer Case

We start our discussion of the integer case by noting that the equation

$$E^4\psi = 0 \tag{A 9}$$

has explicit polynomial solutions of increasing order $2l+1$ ($l \geqslant 0$), as shown in Table 1. Of those, z, z^3, and r^2z satisfy (A 9) as well as all boundary conditions (2.23); however, z and z^3 produce a singular velocity component v_r and must therefore be excluded, leaving r^2z as the only solution of order three.

order	**solution** (ψ)
1	z
3	z^3, r^2z
5	r^4z, r^2z^3
7	$2r^4z^3 - r^6z, 8r^2z^5 - 5r^6z$
9	$48r^4z^5 - 80r^6z^3 + 15r^8z, 32r^2z^7 - 140r^6z^3 + 35r^8z$

TABLE 1. Polynomial solutions to $E^4\psi = 0$ of order $2l+1$, $l \geqslant 0$, in cylindrical coordinates, even in r and odd in z.

Regarding the generic case of $l \geqslant 2$: for the solution to exhibit the correct symmetry, we require even powers in r and odd powers in z, of which there are l monomials. Then, of the boundary conditions (2.23), the first two symmetry conditions and the vanishing shear stress condition are satisfied automatically. Condition (A 9) produces $l-2$ linear equations for the coefficients, so that there are $l-(l-2) = 2$ monomials left at each order which satisfy the equation. Thus, the general solution is a linear combination of these two solutions.

exponent	**solution** (ψ)
1	r^2z
2	$r^2z(r^2 - 4z^2 - 1)$
3	$r^2z\left(r^4 - (12z^2+2)r^2 + 8z^4 + 8z^2 + 1\right)$

TABLE 2. Polynomial basis functions of order $2l+1$, $l \geqslant 1$, satisfying (A 9) and (2.23), with exponent $\lambda = l$ near the tip.

By using a linear combination of the two solutions shown in Table 1 at each order, we ensure that the normal stress boundary condition of (2.23) is also satisfied. We further combine these with solutions of lower order so that ψ exhibits an increasing power-law behavior with an integer exponent $\lambda = l$ at the cusp tip.

REFERENCES

Aarts, D. G. A. L., Lekkerkerker, H. N. W. & H. Guo, G. H. Wegdam, D. Bonn 2005 Hydrodynamics of droplet coalescence. *Phys. Rev. Lett.* **95**, 164503.

Abramowitz, M. & Stegun, I. A. 1968 *Handbook of Mathematical Functions*. Dover.

Anthony, C. R., Harris, M. T. & Basaran, O. A. 2020 Initial regime of drop coalescence. *Phys. Rev. Fluids* **5**, 033608.

Anthony, C. R., Wee, H., Garg, V., Thete, S. S., Kamat, P. M., Wagoner, B. W., Wilkes, E. D., Notz, P. K., Chen, A. U., Suryo, R., Sambath, K., Panditaratne, J. C., Liao, Y.-C. & Basaran, O. A. 2023 Singularities: Breakup and coalescence. *Annu. Rev. Fluid Mech.* **55**, 707.

Brandão, R., Eggers, J. & Fontelos, M. A. 2026 Local cusp solutions of viscous flow. *J. Fluid Mech.* **1029**, A44.

Crowdy, D. & Tanveer, S. 1998 A theory of exact solutions for annular viscous blobs. *J. Nonlinear Sci.* **8**, 375–400.

Deblais, A., Xie, K., Lewin-Jones, P., Herrada, M. A., Eggers, J., Sprittles, J. E. & Bonn, D. 2025 Early stages of drop coalescence. *Phys. Rev. Fluids* **10**, L042001.

Eggers, J. 1993 Universal pinching of 3D axisymmetric free-surface flow. *Phys. Rev. Lett.* **71**, 3458–3460.

Eggers, J. 2023 Viscous free surface cusps - local solution. *Phys. Rev. Fluids* **8**, 124001.

Eggers, J. & Fontelos, M. A. 2005 Isolated inertialess drops cannot break up. *J. Fluid Mech.* **530**, 177–180.

Eggers, J. & Fontelos, M. A. 2015 *Singularities: Formation, Structure, and Propagation*. Cambridge University Press, Cambridge.

Eggers, J., Lister, J. R. & Stone, H. A. 1999 Coalescence of liquid drops. *J. Fluid Mech.* **401**, 293–310.

Eggers, J., Sprittles, J. E. & Snoeijer, J. H. 2025 Coalescence dynamics. *Annu. Rev. Fluid Mech.* **57**, 61.

Frenkel, J. 1945 Viscous flow of crystalline bodies under the action of surface tension. *J. Phys. (Moscow)* **9**, 385.

Gillow, K. 1998 Codimension-two free boundary problems. PhD thesis, Oxford University.

Gradshteyn, I. S. & Ryzhik, I. M. 1980 *Table of Integrals Series and Products*. Academic: New York.

Happel, J. & Brenner, H. 1983 *Low Reynolds Number Hydrodynamics*. Martinus Nijhoff Publishers, The Hague.

Hopper, R. W. 1990 Plane Stokes flow driven by capillarity on a free surface. *J. Fluid Mech.* **213**, 349.

Hopper, R. W. 1991 Plane Stokes flow driven by capillarity on a free surface. part 2. Further developments. *J. Fluid Mech.* **230**, 355.

Hopper, R. W. 1993*a* Capillarity-driven plane Stokes flow exterior to a parabola. *Q. J. Mech. appl. Math.* **46**, 193.

Hopper, R. W. 1993*b* Coalescence of two equal cylinders - Exact results for creeping viscous plane flow driven by capillarity. *J. Am. Ceram. Soc.* **67**, C262.

Hopper, R. W. 1993*c* Coalescence of two viscous cylinders by capillarity: Part I, theory. *J. Am. Ceram. Soc.* **76**, 2947.

Howison, S. D., Morgan, J. D. & Ockendon, J. R. 1997 A class of codimension-two free boundary problems. *SIAM Rev.* **39**, 221–253.

Jeong, J.-T. & Moffatt, H. K. 1992 Free-surface cusps associated with a flow at low Reynolds numbers. *J. Fluid Mech.* **241**, 1–22.

Menchaca-Rocha, A., Martinez-Davalos, A., Nunez, R., Popinet, S. & Zaleski, S. 2001 Coalescence of liquid drops by surface tension. *Phys. Rev. E* **63**, 046309.

Morgan, J. D. 1994 Codimension-two free boundary problems. PhD thesis, Oxford University.

Munro, J. 2018 Coalescence of bubbles and drops. PhD thesis, University of Cambridge.

Paulsen, J. D. 2013 Approach and coalescence of liquid drops in air. *Phys. Rev. E* **88**, 063010.

Paulsen, J. D., Burton, J. C. & Nagel, S. R. 2011 Viscous to inertial crossover in liquid drop coalescence. *Phys. Rev. Lett.* **106**, 114501.

Paulsen, J. D., Burton, J. C., Nagel, S. R., Appathurai, S., Harris, M. T. & Basaran,

O. A. 2012 The inexorable resistance of inertia determines the initial regime of drop coalescence. *PNAS* **109**, 6857.

Pozrikidis, C. 1992 *Boundary Integral and singularity methods for linearized flow*. Cambridge University Press, Cambridge.

Sprittles, J. E. & Shikhmurzaev, Y. D. 2012*a* Coalescence of liquid drops: Different models versus experiment. *Phys. Fluids* **24**, 122105.

Sprittles, J. E. & Shikhmurzaev, Y. D. 2012*b* Finite element framework for describing dynamic wetting phenomena. *Int. J. Numer. Meth. Fl.* **68**, 1257–1298.

Sprittles, J. E. & Shikhmurzaev, Y. D. 2014 A parametric study of the coalescence of liquid drops in a viscous gas. *J. Fluid Mech.* **753**, 279–306.

Thoroddsen, S. T., Takehara, K. & Etoh, T. G. 2005 The coalescence speed of a pendent and a sessile drop. *J. Fluid Mech.* **527**, 85.

Xia, X., He, C. & Zhang, P. 2019 Universality in the viscous-to-inertial coalescence of liquid droplets. *PNAS* **116**, 23467.